remote sensing

MDPI

Article

Assimilating FY-3D MWHS2 Radiance Data to Predict Typhoon Muifa Based on Different Initial Background Conditions and Fast Radiative Transfer Models

Lizhen Huang [1], Dongmei Xu [1,2,*], Hong Li [3], Lipeng Jiang [4] and Aiqing Shu [1]

[1] Key Laboratory of Meteorological Disaster, Ministry of Education (KLME)/Joint International Research Laboratory of Climate and Environment Change (ILCEC)/Collaborative Innovation Center on Forecast and Evaluation of Meteorological Disasters (CIC-FEMD), Nanjing University of Information Science & Technology, Nanjing 210044, China; 202212010158@nuist.edu.cn (L.H.); 20211201033@nuist.edu.cn (A.S.)
[2] State Key Laboratory of Numerical Modeling for Atmospheric Sciences and Geophysical Fluid Dynamics (LASG), Institute of Atmospheric Physics (IAP), Chinese Academy of Sciences (CAS), Beijing 100029, China
[3] Shanghai Typhoon Institute, China Meteorological Administration, Shanghai 200030, China; lih@typhoon.org.cn
[4] State Key Laboratory of Severe Weather, Chinese Academy of Meteorological Sciences, Beijing 100081, China; jianglp@cma.gov.cn
* Correspondence: dmxu@nuist.edu.cn

Abstract: In this study, the impact of assimilating MWHS2 radiance data under different background conditions on the analyses and deterministic prediction of the Super Typhoon Muifa case, which hit China in 2022, was explored. The fifth-generation European Centre for Medium-Range Weather Forecasts (ECMWF) Reanalysis v5 (ERA5) data and the Global Forecast System (GFS) analysis data from the National Centers for Environmental Prediction (NCEP) were used as the background fields. To assimilate the Microwave Humidity Sounder II (MWHS2) radiance data into the numerical simulation experiments, the Weather Research and Forecasting (WRF) model and its three-dimensional variational data assimilation system were employed. The results show that after the data assimilation, the standard deviation and root-mean-square error of the analysis significantly decrease relative to the observation, indicating the effectiveness of the assimilation process with both background fields. In the MWHS_GFS experiment, a subtropical high-pressure deviation to the east is observed around the typhoon, resulting in its northeast movement. In the differential field of the MWHS_ERA experiment, negative sea-level pressure differences around the typhoon are observed, which increases its intensity. In the deterministic predictions, assimilating the FY3D MWHS2 radiance data reduces the typhoon track error in the MWHS_GFS experiment and the typhoon intensity error in the MWHS_ERA experiment. In addition, it is found that the Community Radiative Transfer Model (CRTM) and the Radiative Transfer for Tovs (RTTOV) model show similar performance in assimilating MWHS2 radiance data for this typhoon case. It seems that the data assimilation experiment with the CRTM significantly reduces the typhoon track error than the experiment with the RTTOV model does, while the intensity error of both experiments is rather comparable.

Keywords: background field; MWHS2 radiance; data assimilation; clear sky

check for updates

Citation: Huang, L.; Xu, D.; Li, H.; Jiang, L.; Shu, A. Assimilating FY-3D MWHS2 Radiance Data to Predict Typhoon Muifa Based on Different Initial Background Conditions and Fast Radiative Transfer Models. *Remote Sens.* **2023**, *15*, 3220. https://doi.org/10.3390/rs15133220

Academic Editor: Seon Ki Park

Received: 7 May 2023
Revised: 7 June 2023
Accepted: 15 June 2023
Published: 21 June 2023

Copyright: © 2023 by the authors. Licensee MDPI, Basel, Switzerland. This article is an open access article distributed under the terms and conditions of the Creative Commons Attribution (CC BY) license (https://creativecommons.org/licenses/by/4.0/).

1. Introduction

Intense low-pressure vortex systems known as typhoons are formed in the atmosphere over tropical oceans and often cause disasters, such as strong winds, heavy rainfall, and other related events [1,2]. Accurate forecasting of typhoon track and intensity is of great significance in reducing the enormous losses they cause in terms of assets, human casualties, and economic impacts [3]. In recent years, the utilization of radiance data from microwave

sounders has emerged as a crucial aspect in studies concerning numerical weather prediction (NWP) and its correlation with climate [4,5]. Several microwave sounders have been developed and employed for atmospheric observations. These comprise the Advanced Microwave Sounding Unit-A (AMSUA) [6,7], the Megha-Tropiques/Sounder for Probing Vertical Profiles of Humidity (SAPHIR) [8,9], as well as the NOAA-18 and MetOp-A Microwave Humidity Sounder (MHS) [7]. Additionally, the Advanced Technology Microwave Sounder (ATMS) [10], the GPM Microwave Imager (GMI) on Global Precipitation Measurement (GPM) [11], the Microwave Humidity Sounder (MWHS) on board the FY-3A and FY-3B satellites [12,13], and the Microwave Humidity Sounder II (MWHS2) located on the FY-3C and FY-3D satellites have also been utilized for this purpose. In these radiance observations focusing on China, the FY-3C/FY-3D satellites' MWHS2 is crucial for providing atmospheric temperature and humidity profiles and is widely used for typhoon forecasting [14]. Lawrence et al. [15] assessed the MWHS2 on board the FY-3C satellite in terms of long-term performance using the European Centre for Medium-Range Weather Forecasts (ECMWF)'s NWP system. They determined that its data quality is appropriate for the majority of channels. Their later research showed that MWHS2 provides valuable data for weather forecasting and that assimilating its data into NWP can improve forecast accuracy, particularly for humidity and wind [16]. The MWHS2 channels also have better characteristics, such as resolution and width, in comparison to other microwave detectors with comparable frequency bands [17].

A number of studies have shown that assimilating MWHS and MWHS2 radiance data positively impacts typhoon and precipitation forecasting. Typically, in the process of assimilation, a single reanalysis is utilized as the background field. For example, Yang et al. [12] explored the impact of assimilating FY-3A MWHS data with GFS data as the background field on the numerical prediction of typhoons. By directly assimilating the microwave data, significant improvements were observed in the initial fields of the numerical model, particularly over the ocean where conventional observations were lacking. The assimilated data enhanced the representation of typhoon circulation, temperature, and humidity conditions, leading to more accurate track forecasting. In Xu et al., (2016) [13], an assessment was made regarding the effect of the FY-3B MWHS data on the analysis and predictions of two typhoons, Chan-hom and Linfa. Assimilation of the MWHS data led to improved wind, temperature, and humidity fields, resulting in more accurate predictions of typhoon prediction, intensity, and track than the control experiment. With the launch of the FY-3D and FY-3C satellites, MWHS2 observations are becoming more crucial to assimilation systems. In their research on assimilating FY-3C MWHS2 data, Chen et al. [18,19] made essential contributions. The effect of MWHS2/FY-3C data assimilation using a dynamic emissivity retrieved on precipitation forecast over a complex terrain was examined by Chen et al. [18]. Their results indicated that, with the exception of rainfall above 100 mm, employing the dynamic emissivity retrieved from an 89 GHz channel improved the initial fields and the 24 h forecast of intensity and precipitation distribution. The influence of assimilated FY-3C MWHS2 radiance on Typhoon Hagupit forecast was evaluated by Chen et al. [19] with FNL analysis data as the background field, and they found that it contributed to the improved analysis of wind fields, relative humidity, and temperature, thus improving the typhoon track and intensity forecast. In addition, the effect of assimilation of MWHS2 data from the FY-3C on the analysis and forecasting of binary typhoons was investigated by Xian et al. [20] with FNL reanalysis data as the background field. The findings of their study indicated that there was an enhancement in the humidity and vertical structures of temperature surrounding the central regions of the two typhoons, which consequently led to an improvement in the forecasts of wind, temperature, and humidity. The simulated tracks exhibited a notable resemblance to the observations, leading to a reduction in the margin of error in the estimation of typhoon intensity. With the Global Forecast System (GFS) data as the background field, Sun and Xu [21] studied the effect of assimilating MWHS2 data on board the FY-3D satellite in predicting heavy rainfall related to Typhoon Ampil. The MWHS2 data assimilation considerably improved the position and rainfall

forecast accuracy of the typhoon, according to their findings. The influence of assimilating FY3D MWHS2 data for Typhoon Ampil forecasting using the three-dimensional variation (3DVAR) method was examined by Xu et al. [22]. They noticed that the height and humidity fields were significantly improved, which improved the accuracy of precipitation and track forecasting. It appears that the use of MWHS2 radiance with GFS data can better improve the analysis of tropical cyclone structure and humidity conditions [23,24]. Moreover, MWHS2 not only improves typhoon forecasts but also improves the accuracy of precipitation forecasts [18,25].

On the other hand, different results can be produced due to the iteration of two different initial fields in the chaotic atmospheric dynamic function [26]. The analysis field is closely related to the driving field selected by the model under consideration when assimilating the determined model and the same satellite data. Currently, the influence of different driving fields on assimilation and prediction is not comprehensively studied in microwave sounder radiance data assimilations, especially for typhoons [27]. A recent study using different initial fields for data assimilation based on the Japan Meteorological Agency (JMA) and GFS reanalysis data as the background fields found that utilizing the JMA reanalysis data as the background field resulted in a more remarkable improvement in predicting typhoon precipitation, track, and intensity than using the GFS data [28]. From the progress of previous studies, the sensitivity of the effect of radiance data assimilation still seems uncertain in terms of using different background conditions for improving the initial field and deterministic prediction of typhoons. Building upon these findings, this study explored the assimilation impacts of FY3D MWHS2 radiances on the prediction of Typhoon Muifa. This was achieved through the implementation of the 3DVAR method using GFS analysis data and ERA-5 reanalysis data as the background fields. During the course of the investigation, a comparative analysis was conducted between the Radiative Transfer for Tovs (RTTOV) observation operator and the Community Radiative Transfer Model (CRTM) observation operator in order to facilitate the comprehension of the impacts caused by radiative transfer. The findings of this study could enhance our knowledge of how the MWHS2 affects typhoon prediction and provide valuable insights for assessing MWHS radiances on the FY3D satellite.

In the subsequent sections of the paper, an exposition of the observations and the 3DVAR method is presented in Section 2. The experimental design is expounded in Section 3, which is accompanied by a comprehensive depiction of the typhoon itself. The outcomes of assimilating the FY3D MWHS2 radiance data are presented in Section 4. Section 5 compares the different effects of MWHS2 data assimilation via the RTTOV and CRTM observation operators on Typhoon Muifa forecasts. In Sections 6 and 7, discussions and conclusions are offered, respectively.

2. Materials and Methods

2.1. Observations

2.1.1. MWHS2 Radiance Data

The fourth meteorological satellite in China's FY-3 series, FY-3D, was successfully launched on 15 November 2017. Together with the FY-3C, it forms a joint morning and afternoon observation network for all-weather and global Earth observations. The FY-3D carries the Microwave Humidity Sounder II (MWHS2) and other instruments. Compared to the previous-generation MWHS carried on the FY-3A/B, the MWHS2 has been upgraded with more detection channels and higher spatial accuracy [29]. The MWHS2 detector owns 15 channels, including channels (11–15) with a central frequency of 183.31 GHz and channels (2–9) with a central frequency of 118.75 GHz, and another 2 window channels (1 and 10). It should be pointed out that the error limits stand for the varying range of central frequency for each channel. Additionally, five of these channels are employed to detect the vertical distribution of humidity in the atmosphere [20]. The assimilation of radiance in this study was limited to channels 11, 12, 13, 14, and 15, which were chosen based on the information presented in Table 1 concerning the MWHS2's various channels.

Table 1. Peculiarities of the multiple channels in the MWHS2.

Channel	Central Frequency (GHZ)	Bandwidth (MHz)	Frequency Stability (K)	Resolution (km)
1	89	1500	50	25
2	118.75 ± 0.08	20	30	25
3	118.75 ± 0.2	100	30	25
4	118.75 ± 0.3	165	30	25
5	118.75 ± 0.8	200	30	25
6	118.75 ± 1.1	200	30	25
7	118.75 ± 2.5	200	30	25
8	118.75 ± 3.0	1000	30	25
9	118.75 ± 5.0	2000	30	25
10	150	1500	50	15
11	183.31 ± 1	500	30	15
12	183.31 ± 1.8	700	30	15
13	183.31 ± 3	1000	30	15
14	183.31 ± 4.5	2000	30	15
15	183.31 ± 7	2000	30	15

2.1.2. Conventional and Precipitation Observation

The data employed in this research were obtained from a heterogeneous range of sources via the Global Telecommunications System (GTS), encompassing radiosonde, aircraft reports, land surface, and atmospheric motion vectors.

The China Land Data Assimilation System (CLDAS)'s multi-source precipitation fusion dataset, comprising an analysis product of hourly precipitation with a resolution of $0.0625^\circ \times 0.0625^\circ$ covering the region of China, provided the precipitation data employed for verification in this research.

2.2. Background Fields

To compare the effects of different background field conditions on MWHS2 radiance data assimilation, this study selected two sets of data to initialize the background fields, GFS and ERA5. The GFS dataset leverages a sophisticated global data assimilation system and an extensive database, which are constructed collaboratively by the National Center for Atmospheric Research and the National Centers for Environmental Prediction. The data possess a resolution of $0.25^\circ \times 0.25^\circ$ and are derived from the Global Data Assimilation System (GDAS). The other dataset comprises the fifth-generation ECMWF Reanalysis v5 (ERA5) data, which have a $0.25^\circ \times 0.25^\circ$ spatial precision.

2.3. WRFDA Assimilation System

WRFDA, the data assimilation system of the WRF model, offers a diverse range of assimilation methods, encompassing 3DVar, hybrid assimilation, four-dimensional variation (4DVar), and many other methods. For this investigation, the cost function $J(\mathbf{x})$ is iteratively minimized in order to gain an optimal analysis of the current atmospheric state:

$$J(\mathbf{x}) = (\mathbf{x} - \mathbf{x_b})^T \boldsymbol{B}^{-1} (\mathbf{x} - \mathbf{x_b}) + \left[\mathbf{y}_0 - \boldsymbol{H}(\mathbf{x})\right]^T \boldsymbol{R}^{-1} [\mathbf{y}_0 - \boldsymbol{H}(\mathbf{x})], \quad (1)$$

The atmospheric current condition is represented by the analysis vector $\mathbf{x}$ updated through assimilation, which is previously provided by the background vector $\mathbf{x_b}$. The matrix $\boldsymbol{B}$ is a representation of the covariance of background error. It is produced through

the one-month National Meteorological Center (NMC) method and helps to capture the uncertainty in the background estimate. Real-world atmospheric data collected from various sources are represented by the observation vector $\mathbf{y}_0$, and the observation error covariance matrix $\boldsymbol{R}$ quantifies the level of uncertainty inherent in these observations. The transformation of the atmospheric state from the model to the observation space is achieved through the use of a nonlinear observation operator $\boldsymbol{H}$. To estimate the observation error for this study, the observation error $\boldsymbol{R}$ is calculated for each channel for roughly one week at every 6 h utilizing the standard deviation of the difference between the observed and the simulated brightness temperature based on the initial GFS analysis data or the ERA-5 reanalysis data.

2.4. MWHS2 Radiance Data Assimilation Method

To assimilate the MWHS2 radiance data in this study, the RTTOV was first applied as the observation operator. In addition, as described in Section 5, as an observation operator to be compared with the RTTOV, the CRTM was employed, thus increasing the comprehensiveness of the study. The WRFDA procedure incorporated multiple quality control measures. Specifically, observations were excluded if they had brightness temperature (BT) values below 50 K or above 550 K, observation residuals exceeding 15 K, or residuals after bias correction that were three times higher the observation standard deviation σ_0. Only observations in clear-sky regions were retained for clear-sky data assimilation. Those cloud-contaminated data were excluded in cloudy areas, where a scattering index was greater than 5 K, or a liquid cloud water path's value was greater than $0.2 \mathrm{g \cdot m^{-2}}$. Observations were also excluded for land or overly complex surface types in the WRF model's terrain file on the ocean surface.

Upon the completion of quality control procedures, it is imperative to address any systematic biases present in satellite data. One such bias present in radiance data can be represented through a linear combination of specific predictors [30] as follows:

$$\widetilde{H}(\boldsymbol{x}, \boldsymbol{\beta}) = H(\boldsymbol{x}) + \beta_0 + \sum_{i=1}^{N_p} \beta_i p_i. \quad (2)$$

The formula contains $H(\boldsymbol{x})$ and $\widetilde{H}(\boldsymbol{x}, \boldsymbol{\beta})$ as the observation operators before and after bias correction, respectively. $\boldsymbol{x}$ stands for the model state vector, while the regular part of the total bias is denoted as β_0, and the i-th predictor and bias correction coefficient are expressed as β_i and p_i, respectively. Under the assumption of independent channels, the variational bias correction method, which minimizes offline computation, may be used to gain the bias correction coefficient β_i. The present investigation involved the application of an offline mode of the WRFDA VarBC. To calculate the bias correction coefficient for the assimilation cycle, a half-month offline run was carried out in this research.

3. Typhoon Case and Experimental Design

3.1. Overview of Typhoon Muifa

Typhoon Muifa was the twelfth typhoon in 2022 originating from the northwest Pacific Ocean and the first typhoon to hit East China. It was also the strongest typhoon to hit China as of September in 2022. The backgrounds initialized using the GFS and ERA-5 analysis data for the scanning orbits of MWHS2 radiance simulation are shown in Figure 1. It is found that the second orbit in the east covers the track of Typhoon Muifa as predicted by the CMA. The typhoon formed in the northwest Pacific Ocean at 0000 UTC on 8 September with a strength of 998 hPa. On 14 September, around 1200 UTC, it developed into a severe typhoon as it neared the coast and made landfall in Zhoushan, Zhejiang, with a strength of 960 hPa. Heavy rains caused flooding in northern Zhejiang, Shanghai, Jiangsu, central and eastern Shandong, and the Liaodong Peninsula. Subsequently, Typhoon Muifa hit the coast of Fengxian, Shanghai, a second time at around 1600 UTC on 14 September before gradually turning northeast. It made landfall again at 1600 UTC on September 15 on the coast of Laoshan, Qingdao, Shandong Province, for a third time (tropical storm). Finally, at

0400 UTC on 16 September, it landed again in Jinpu, Dalian, Liaoning Province. Due to surface friction, it weakened into an extratropical cyclone and eventually disappeared in northeast Liaoning at 1200 UTC on 16 September.

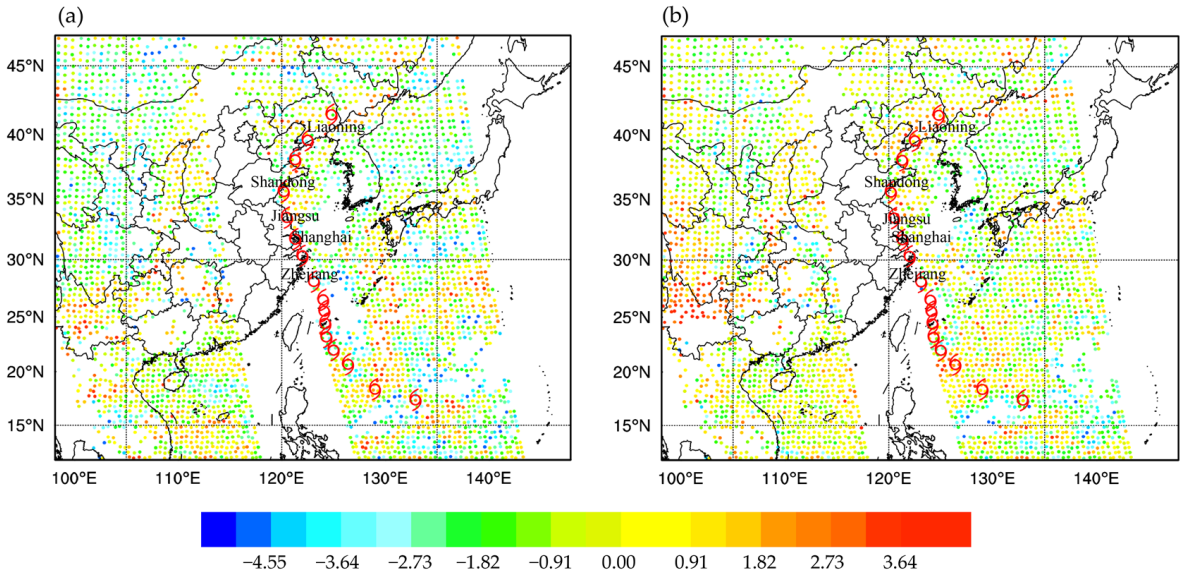


Figure 1. The track of Typhoon Muifa (red symbols) from 000 UTC on September 8 to 0012 UTC on September 16 covered by the scanning orbits (color dots): radiances simulated with the background initialized using the GFS analysis data (**a**) and the ERA-5 reanalysis data (**b**) in the model domain.

Figure 2 displays the circulation patterns in the lower layer and middle layer around the assimilation time based on the Global Forecast System (GFS) analysis data. Typhoon Nanmadol in the east is mostly responsible for the moisture nearby the core of Typhoon Muifa at the lower level. At the middle level, the subtropical high moves northward in a block shape, and in the process of typhoon development, it gradually merges with the continental high. It strengthens, leading to a strengthening of the westward component of the typhoon track. During the activity period of Typhoon Muifa, Typhoon Nanmadol developed into a super typhoon. The presence of dual typhoons can lead to complex track interactions, resulting in significant forecast errors [31]. Therefore, acquiring more accurate initial conditions by assimilating MWHS2 radiance data is crucial for improving the accuracy of typhoon forecasts.

3.2. Experiment Design

The Advanced Research WRF (ARW) version 4.4 was employed to conduct the experiments in this study, which has a horizontal resolution of 9 km and is centered on 31°N and 123°E (Figure 1). The numbers of zonal grids and meridional grids are 559 and 469, respectively. The number of vertical layers is 61, and the pressure at the topmost layer is 10 hPa. The GFS analysis data and ERA-5 reanalysis data with a 0.25° × 0.25° horizontal resolution were utilized to supply the initial and boundary conditions. This study employed some parameterizations such as the WRF Single-Moment 6-Class Microphysics (WSM6) scheme [32], the Yonsei University (YSU) boundary layer scheme [33], the Dudhia short-wave radiation scheme [34], the Rapid Radiative Transfer Model (RRTM) longwave radiation scheme [35], the Noah land surface model, and the Kain–Fritsch cumulus parameterization scheme [36].

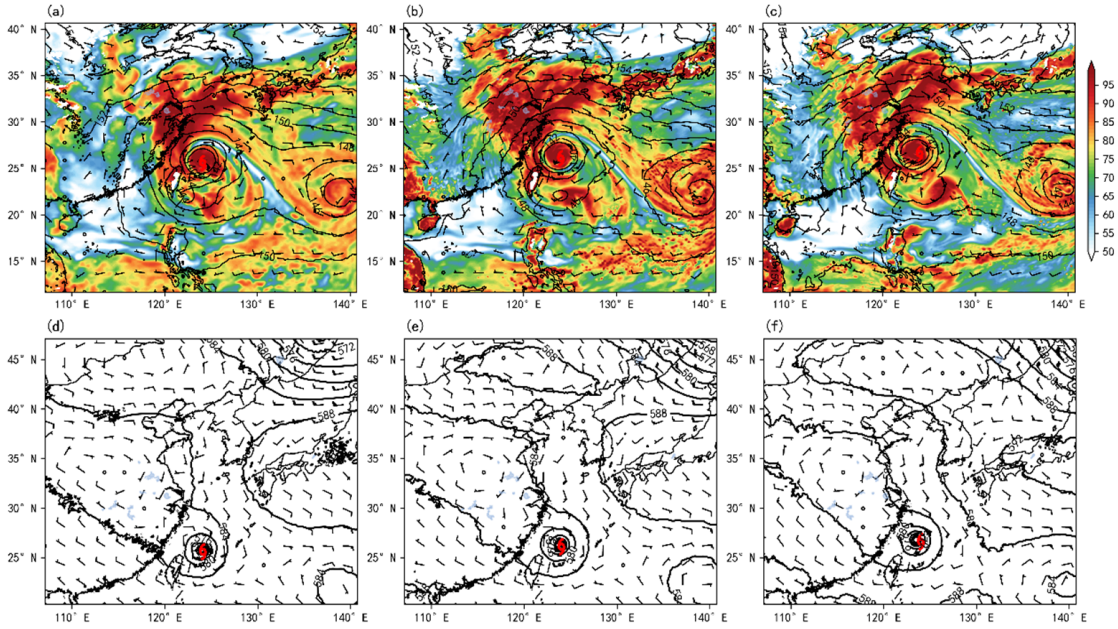


Figure 2. The 850 hPa circulation comprises geopotential height (lines, unit: dagpm), specific humidity (shading, unit: g/kg), and wind field (vectors, unit: m/s) at (**a**) 0000 UTC, (**b**) 0600 UTC, and (**c**) 1200 UTC on 13 September 2022; the 500 hPa circulation encompasses geopotential height (lines, unit: dagpm) and wind field (vectors, units: m/s) at (**d**) 0000 UTC, (**e**) 0600 UTC, and (**f**) 1200 UTC. The red symbol indicates the core of Typhoon Muifa at each appropriate time.

The flowchart for the three main steps of the data assimilation experiments is demonstrated in Figure 3. In order to evaluate the assimilation of MWHS2 radiance, the forecast cycle was run from 0000 UTC on 13 September, soon after Typhoon Muifa was recognized as a severe typhoon, to 0000 UTC on 15 September, soon after Typhoon Muifa landed in Zhejiang. First, at 0000 UTC on 13 September 2022, a six-hour warm start was initiated. Second, the forecast field at 0600 UTC on 13 September 2022 was used as the background to assimilate the GTS and MWHS2 radiance data. Third, from 0600 UTC on 13 September to 0000 UTC on 15 September, a final 42 h deterministic forecast was conducted. For comparison, four experiments were performed. The first two experiments served as the controls, in which only the GTS data were assimilated with either the GFS analysis data (GTS_GFS) or the ERA-5 reanalysis data (GTS_ERA) as the background field. Figure 4 illustrates the distribution of the GTS observation data at 0600 UTC on 13 September 2022. Based on the first two experiments, the third and fourth experiments assimilated both the GTS and MWHS2 radiance data. The GFS background field was applied in the third experiment and named as MWHS_GFS, while the fourth experiment used the ERA-5 background field called MWHS_ERA. The MWHS2 radiance data in its original form were subjected to thinning on a 54 km grid in order to present possible correlations between adjoining radiance observations.

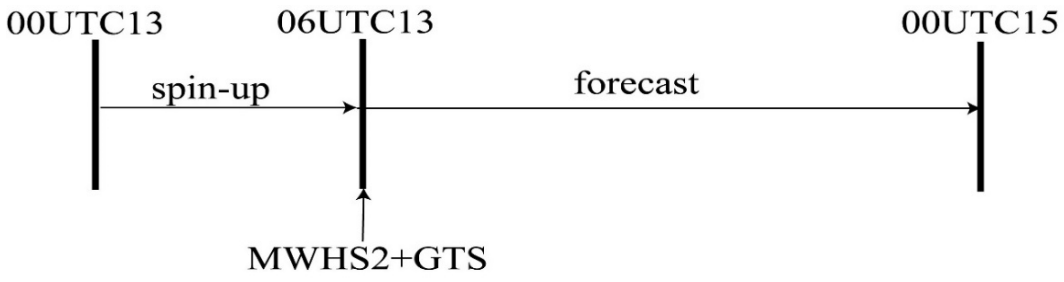


Figure 3. The flow chart for the data assimilation experiments.

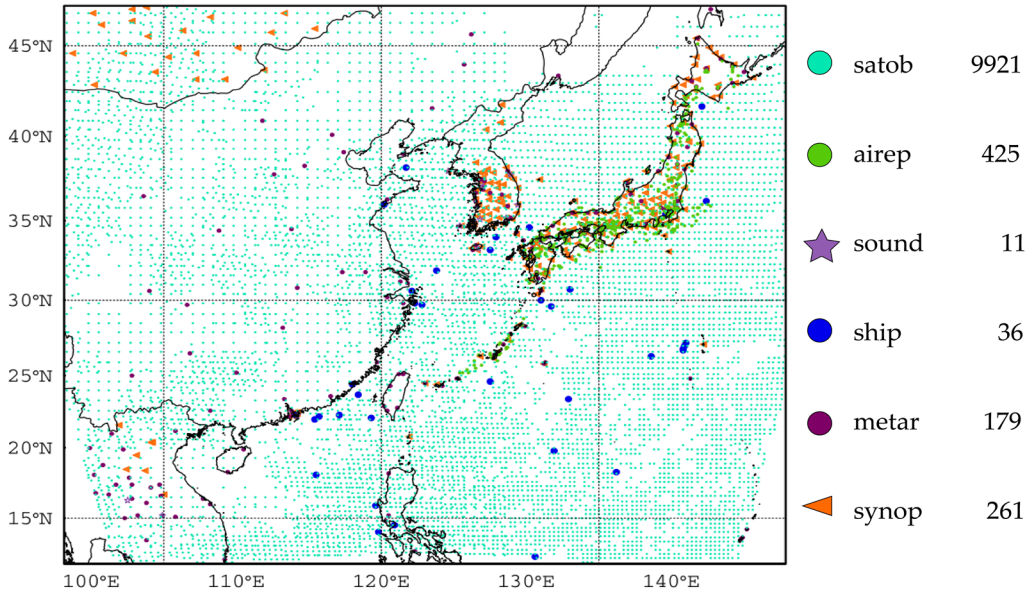


Figure 4. Distribution of GTS observations, including radiosondes (sound), ship, satellite atmospheric motion vector (satob), meteorological aerodrome reports (metar), aircraft reports (airep), and surface synoptic observations (synop), at 0600 UTC on 13 September 2022.

4. Results Based on Different Initial Fields

4.1. Bias Correction

Focusing on the impacts of MWHS2 radiance, the scatter plots in Figure 5 portray the simulated and the observed brightness temperature (BT) at 0600 UTC on 13 September 2022, before and after the bias adjustment in the experiments using the GFS and ERA-5 analysis data. As observed from the GFS experiment, the bias of OMB is −2.744 K (Figure 5a). The bias of OMB is significantly lower (−0.544 K) after bias correction. It further decreases to −0.150 K after assimilation. Additionally, the RMSE and standard deviation similarly decrease from 1.976 K and 1.900 K to 0.252 K and 0.202 K, respectively (Figure 5b,c). Similarly, in the ERA-5 experiment, the simulated values of the background field exceed the observations prior to the bias correction for the majority of points on the scatter plot (Figure 5d). Subsequently, the systematic bias is primarily eliminated (Figure 5e). Furthermore, following the assimilation of MWHS2, the mean, standard deviation, and RMSE are nearly equal to zero (Figure 5f). According to these results, the data assimilation method is capable of effectively adjusting the moisture information and temperature to match the observations, taking into account both the observations and background errors.

4.2. Impacts of the MWHS2 Data on Analyses

To examine the influence of MWHS2 radiance on TC forecast based on different background conditions, the analysis increments for the GFS and ERA-5 experiments are shown in Figures 6–9.

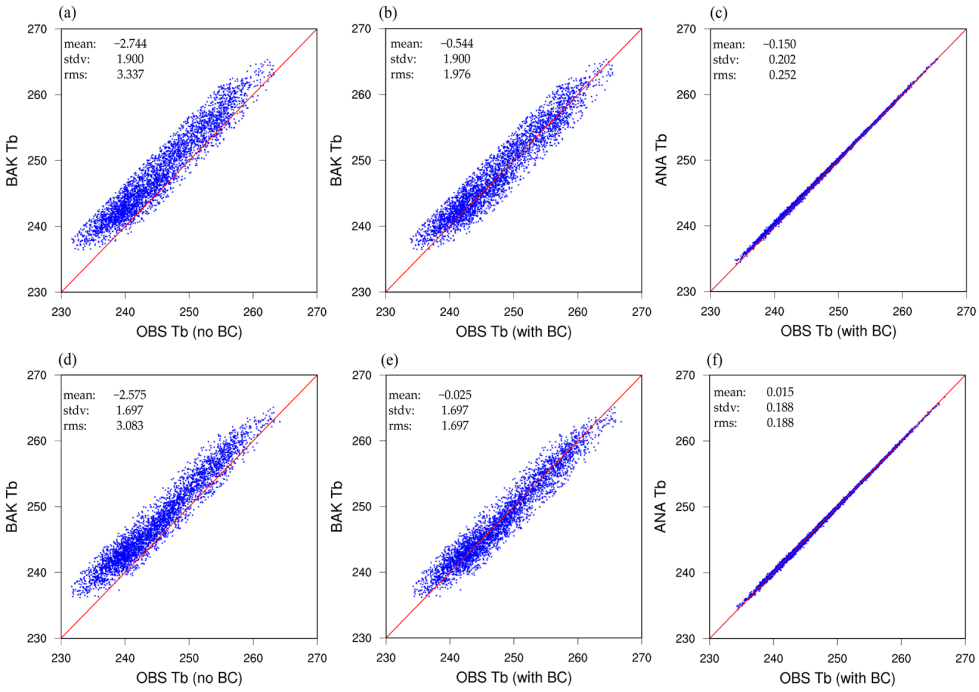


Figure 5. The scatter diagrams of the GFS data as background against observation (**a**) before the bias correction, (**b**) observation after the bias correction, and (**c**) observation from channel 11. The scatter diagrams of the ERA-5 data as background against observations (**d**) before the bias correction, (**e**) after the bias correction, and (**f**) from channel 11 at 0600 UTC on 13 September 2022.

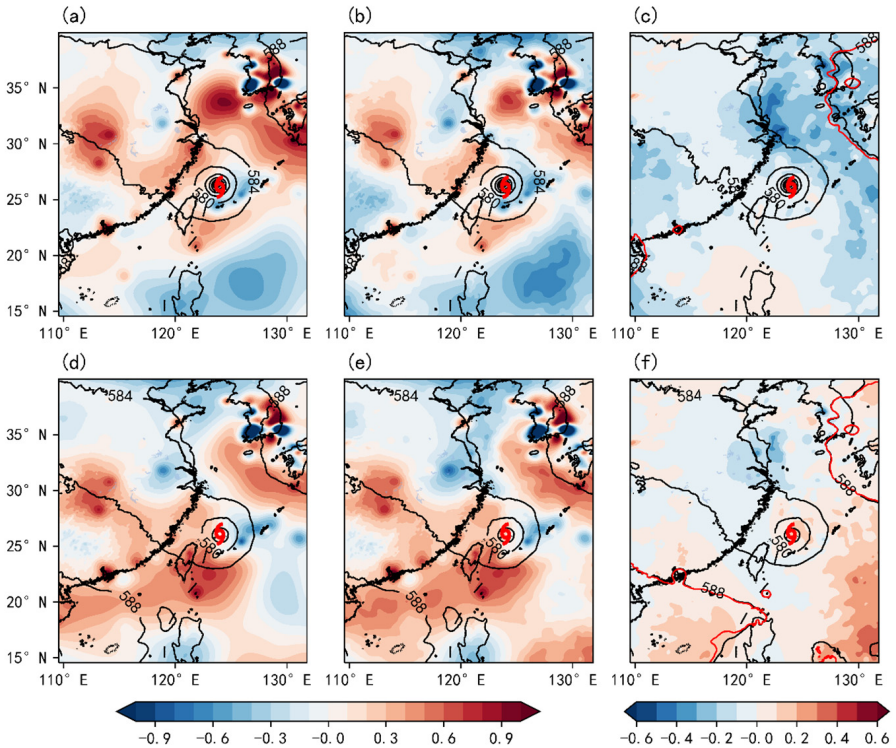


Figure 6. Analysis increments (shading, units: gpm) with a background (contours, units: gpm) of 500 hPa geopotential height in the experiments (**a**) GTS_GFS, (**b**) MWHS_GFS, (**d**) GTS_ERA, and (**e**) MWHS_ERA. (**c**) shows the difference between GTS_GFS and MWHS_GFS, and (**f**) shows the difference between GTS_ERA and MWHS_ERA. Red line: 588 isoline in GTS_GFS and GTS_ERA. The red symbol represents the center of Typhoon Muifa.

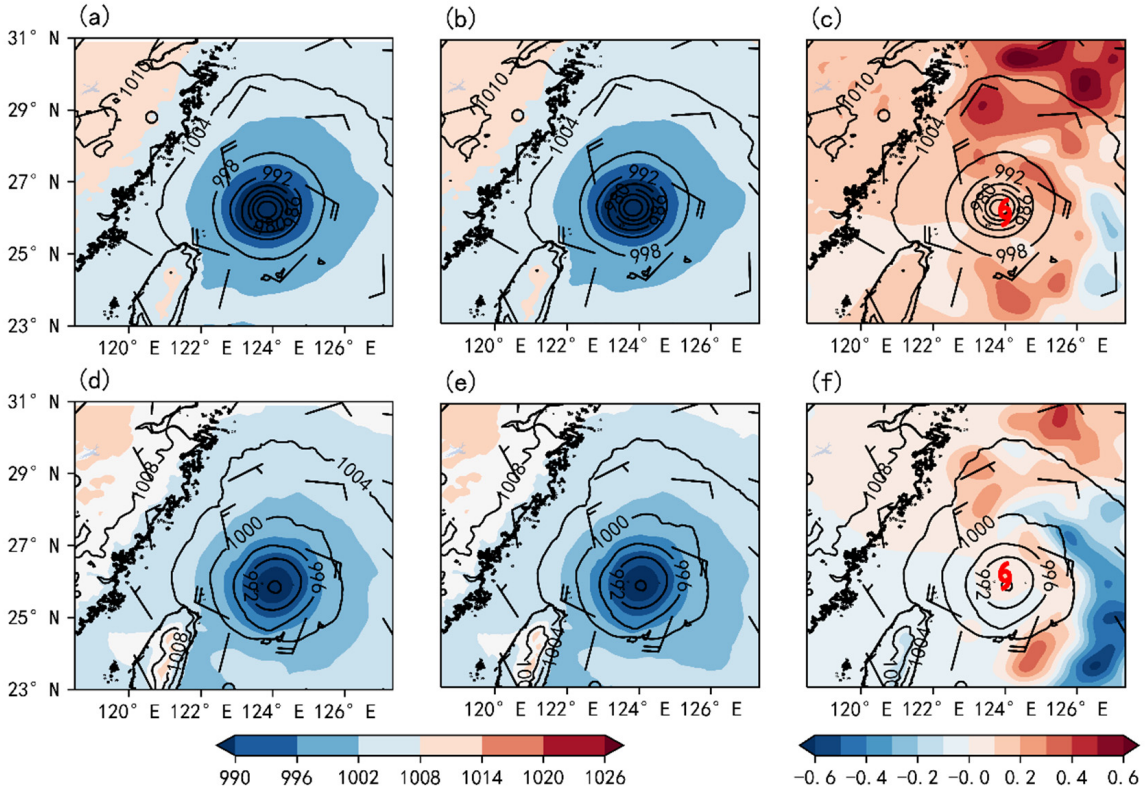


Figure 7. SLP (shading and contours, units: gpm) and the near-surface wind (units: m/s) in the experiments (**a**) GTS_GFS, (**b**) MWHS_GFS, (**d**) GTS_ERA, and (**e**) MWHS_ERA. (**c**) is the difference between GTS_GFS and MWHS_GFS, and (**f**) is the difference between GTS_ERA and MWHS_ERA. The red symbol represents the center of Typhoon Muifa.

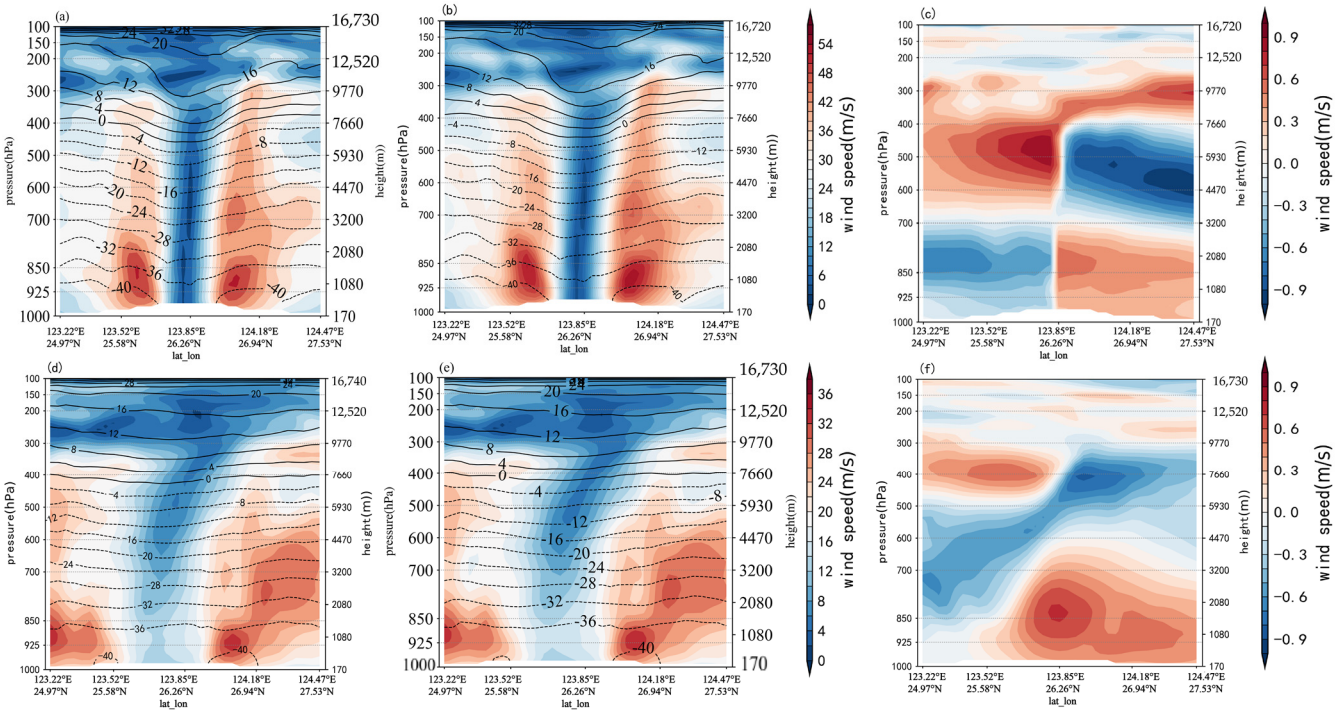


Figure 8. Same as Figure 7, but for potential temperature anomaly (contours, units: K) and horizontal wind (shading, units: m/s).

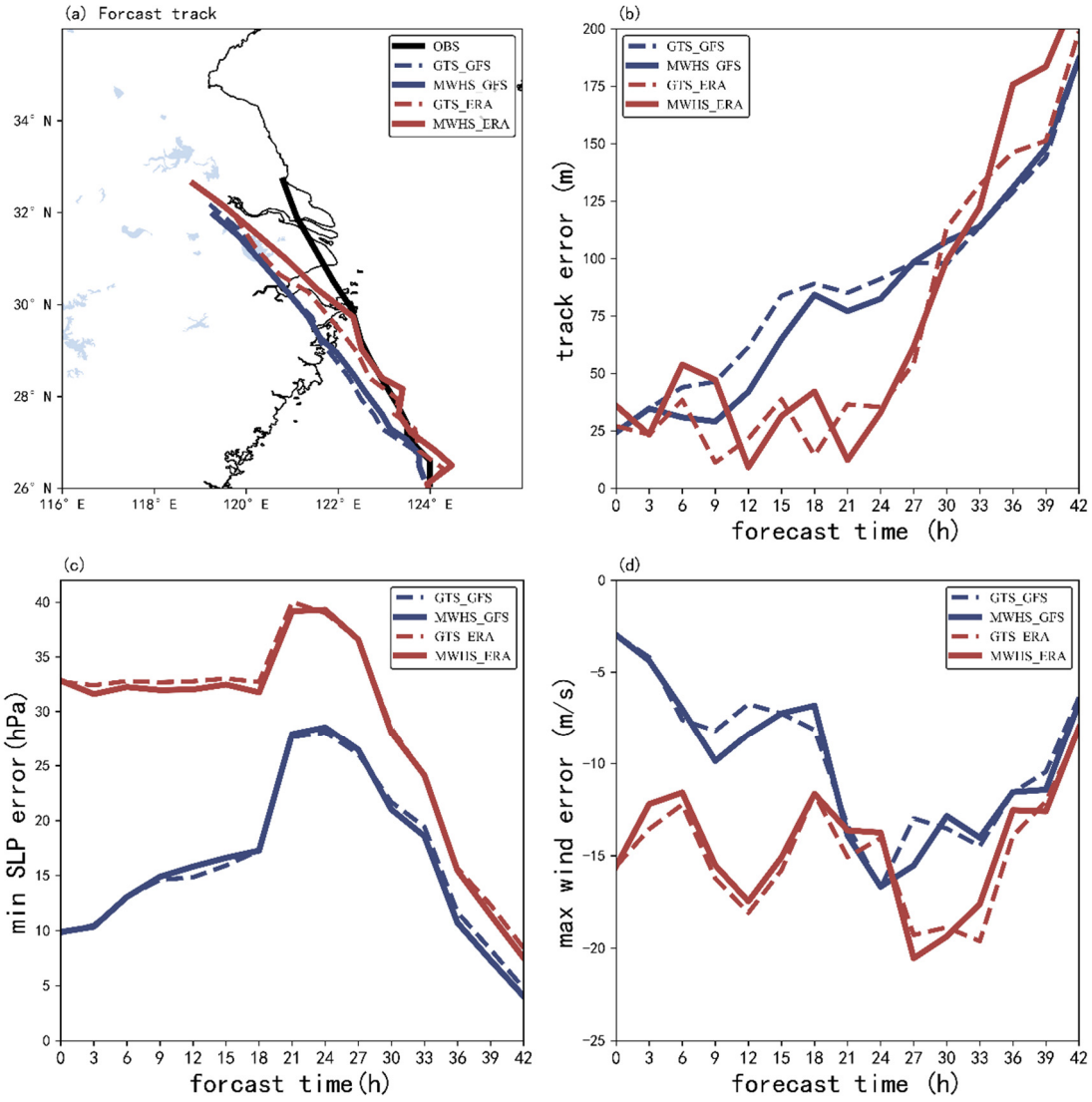


Figure 9. Track forecast (**a**), track error (**b**), MSLP (**c**), and near-surface WS_{max} (**d**) of 42 h deterministic forecast.

4.2.1. Geopotential Height Increment

The 500 hPa geopotential height and geopotential height increment based on the GFS and ERA-5 data at 0600 UTC on 13 September 2022 are displayed in Figure 6. The GTS_GFS experiment illustrates a decrease in height in the southeast and an increase in height toward the southwest of the typhoon for the surrounding environment (Figure 6a). Conversely, a relatively high height is exhibited in the southwest of the typhoon in the GTS_ERA experiment (Figure 6d). Benefiting from this, the typhoon track simulated by the ERA-5 data is biased toward the northeast and closer to the observation compared to the GFS data. In its differential field, the MWHS_GFS experiment indicates a negative difference in height and an increase in the area with negative geopotential height in the north of the typhoon compared to the GTS_GFS experiment. Upon assimilating the MWHS2 data, the black line shifts eastward in comparison to the red line, and the 588 isoline retreats eastward (Figure 6b,c). The typhoon track simulated by the MWHS_GFS experiment is northeastward, indicating that the incorporation of the MWHS2 radiance data through assimilation has a correcting effect on the GFS analysis data's simulated typhoon track. For the MWHS_ERA experiment, the black and red lines almost coincide, and the difference in height is nearly zero (Figure 6e,f). This implies that assimilating the MWHS2 radiance data has little effect on the typhoon track correction simulated by the ERA-5 reanalysis data.

4.2.2. Sea-Level Pressure (SLP) and Near-Surface Wind

Figure 7 demonstrates the sea-level pressure (SLP) and the near-surface wind using the GFS and ERA-5 data. In the GTS_GFS experiment, denser and stronger SLP contours are obtained, reaching a minimum of 968 hPa, while the SLP contours in the GTS_ERA experiment are sparser, with a minimum of only 988 hPa (Figure 7a,d). And the typhoon eye in the GTS_ERA experiment is smaller. Following the assimilation of the MWHS2 radiance data, the MWHS_ERA experiment exhibits an increase in SLP intensity (Figure 7e), with the differential field in Figure 7f being negative in the east of the typhoon. It suggests that assimilating the MWHS2 data efficiently corrects the SLP intensity simulated by the ERA-5 reanalysis data. On the other hand, the SLP difference around the typhoon in Figure 7c is nearly equal to (or larger than) zero, indicating that the correction effect of the MWHS2 radiance data on the GFS analysis data is insignificant.

4.2.3. Potential Temperature Anomaly and Horizontal Wind

The potential temperature anomaly and the horizontal wind are presented in Figure 8. The experiments demonstrate differences in the typhoon eye and the maximum wind speed (WS_{max}) area, with the GTS_GFS experiment yielding a narrower typhoon eye and a WS_{max} of 52 m/s in comparison to 34 m/s in the GTS_ERA experiment. Consistent with those findings in Figure 7, the MWHS_ERA experiment suggests that assimilating the MWHS2 radiance data results in an increase in wind speed, as observed by the positive differential field using the ERA-5 data as the background.

4.3. Impacts of the MWHS2 Data on Forecasts

In Figure 9, the outcomes of the 42 h deterministic forecast from the four experiments are depicted, including the typhoon track and track error compared to observation. At the outset, the deterministic forecast has a 30 km error owing to the 6 h warm-start run. Over the initial 30 h period, the track error in the GTS_ERA experiment is inferior to that of the GTS_GFS experiment, signifying that the simulated track of the ERA-5 reanalysis data aligns more closely with the observation. However, during the final 12 h, the track error escalates abruptly in the GTS_ERA experiment, surpassing the error of the GTS_GFS experiment considerably. A lower track error compared to the GTS_GFS experiment for the first 27 h is exhibited in the MWHS_GFS experiment, indicating that incorporating the MWHS2 data improves the results of the forecast. Conversely, regarding the ERA-5 reanalysis data, there is no apparent distinction between the GTS_ERA experiment and the MWHS_ERA experiment.

Figure 9c,d present the minimum sea-level pressure (MSLP) error and the near-surface WS_{max} error of the four experiments and observations. The lower error in the initial MSLP and near-surface WS_{max} is displayed in the GTS_GFS experiment in comparison to the GTS_ERA experiment. It is found that the GFS analysis data provide a typhoon intensity simulation that better matches the observation. For the first 27 h, the difference between the GTS_GFS and MWHS_GTS experiments is insignificant. However, in the MWHS_ERA experiment, the MSLP and near-surface WS_{max} errors are consistently less than those in the GTS_ERA experiment. This suggests that assimilating the MWHS2 data is able to correct the typhoon intensity simulation to a larger extent when the TC intensity in the background is weak based on the ERA-5 reanalysis data.

5. Results Based on Different Fast Radiative Transfer Models

5.1. Radiance Simulation and Bias Correction

To compare the simulation outcomes of the RTTOV model and the CRTM, the ERA-5 reanalysis data were selected. Figure 10 illustrates the OMB and OMA from channel 11 at 0600 UTC on 13 September 2022. It is important to note that in order to prevent cloud complexity, some of the typhoon's scanning points have been removed. It can be seen in Figure 10 that the number of observations in the CRTM and the RTTOV model is comparable. There are considerable errors in the background BT relative to the observation,

as shown in Figure 10a,d, and the CRTM's mean value (0.16 K) is higher than that of the RTTOV model. However, after assimilating the MWHS2 radiance data, the CRTM yields a smaller mean (0 K) and standard deviation (0.18 K) compared to the RTTOV model, which has a mean and standard deviation of 0.01 K and 0.19 K, respectively. It seems that assimilating the MWHS2 radiance data with the CRTM is more effective.

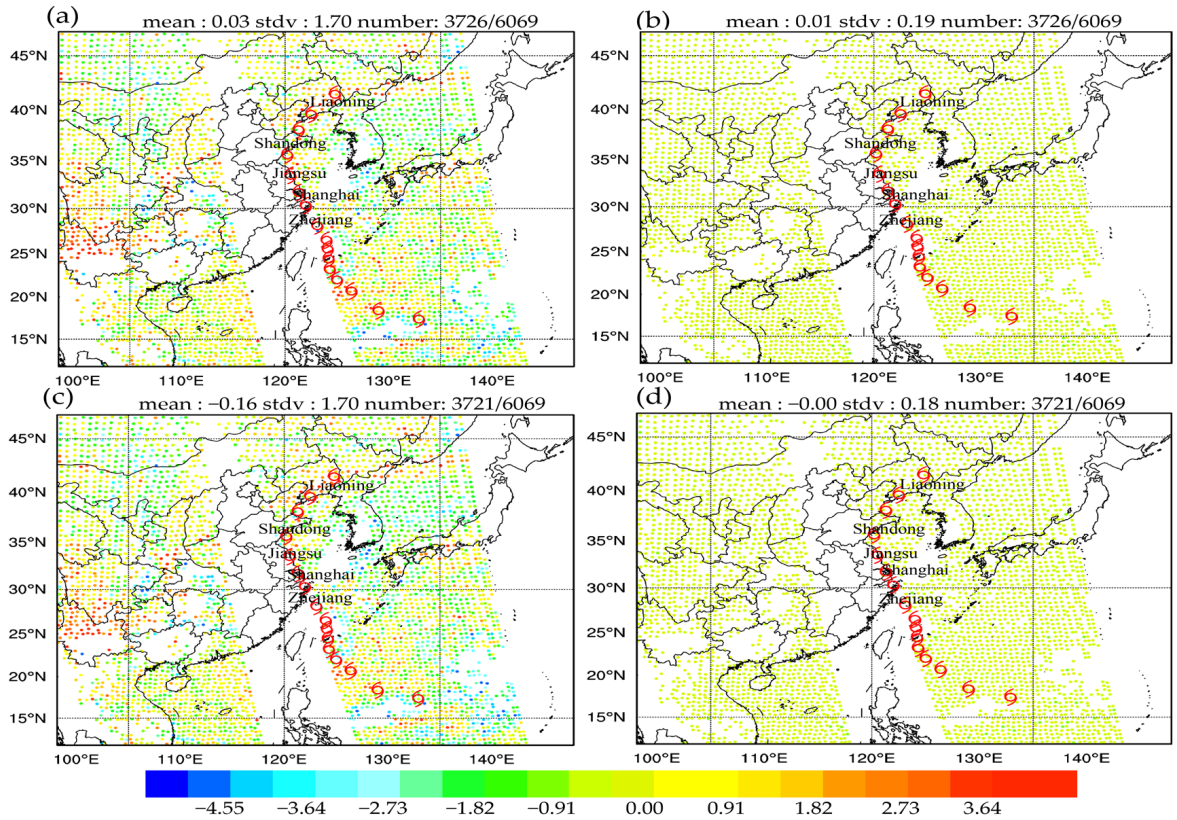


Figure 10. (**a**) The OMB (unit: K) and (**b**) the OMA (unit: K) from the RTTOV model, and (**c**) the OMB (unit: K) and (**d**) the OMA (unit: K) from the CRTM for channel 11 at 0600 UTC on 13 September. The red symbols is the same as Figure 1.

The scatter plots in Figure 11 portray the simulated and observed BT in the RTTOV model and the CRTM at 0600 UTC on 13 September 2022. The majority of scatter points are located above the diagonal line, indicating that the CRTM produces a warmer background BT than the RTTOV model. After the assimilation, the scatter points are arranged equitably along the diagonal. The mean and rmse decrease and approach zero, suggesting that the difference in brightness temperature between the two models is reduced after the assimilation. The possible reason for this difference is that the two models have different ways to calculate the surface emissivity [37]. While the CRTM applies a Specular Reflection model, the reflectivity model employed by the RTTOV model involves the use of Lambertian BRDF.

5.2. Jacobian Functions

Figure 12 depicts the Jacobian functions of water vapor for channels 11–15 using the standard atmosphere as predicted by the RTTOV model and the CRTM. The sensitivity of top-of-atmosphere (TOA) radiance to variations either in the atmospheric or surface water vapor is represented by the Jacobian functions [38]. In the RTTOV model, the peaks of the Jacobian functions are distributed between 500 and 300 hPa, with the most extensive response function observed in channel 11 (Figure 12a). The CRTM also shows similar distribution characteristics to the RTTOV model with some insignificant differences. Specifically, the CRTM shows a decrease in the peak height of channel 11 and slightly lower sensitivity in channels 11–13 to water vapor, whereas channels 14–15 show higher sensitivity

(Figure 12b). This feature of absorption and emission of water vapor leads to an increase in the background brightness temperature for channel 11 (Figure 11a). When considering the total effects of all the channels, it appears that the channels in the CRTM experiment are more sensitive to water vapor than the channels in the RTTOV experiment. This may also lead to a TC analysis with enhanced thermal/dynamical TC and environmental field in the CRTM experiment.

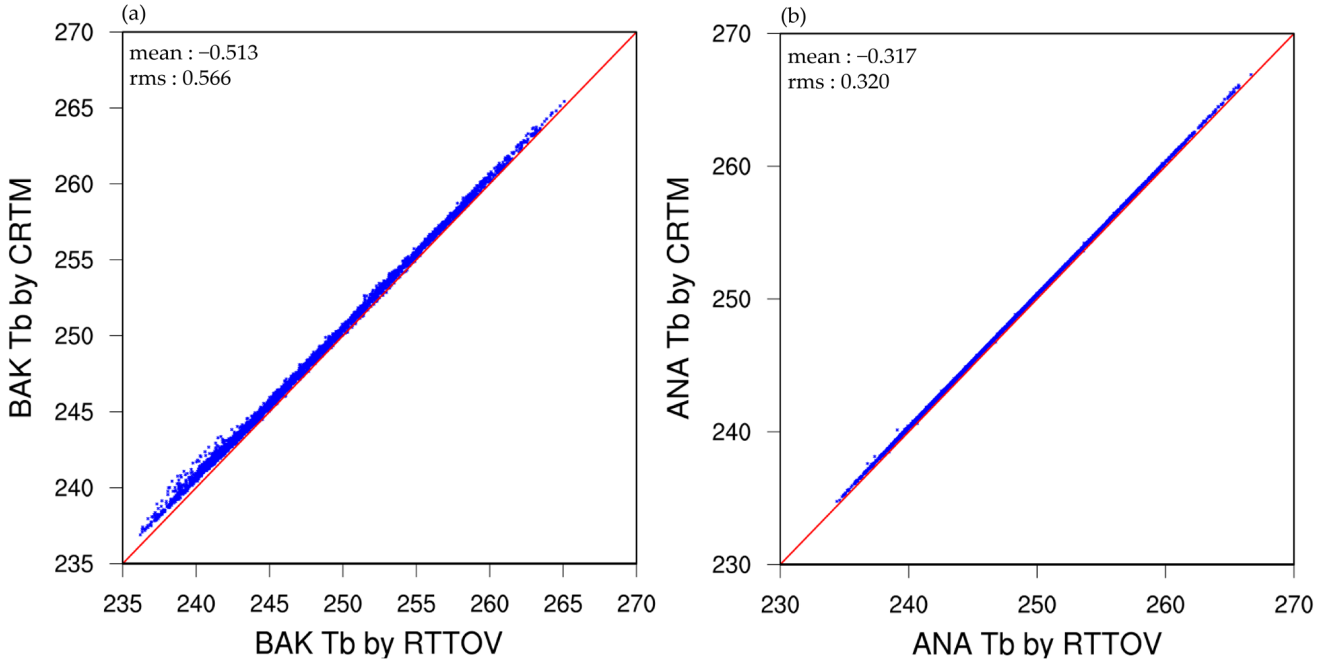


Figure 11. The scatter diagrams of the RTTOV model-simulated BT versus the CRTM-simulated BT (unit: K) of the background (**a**) after the bias correction, and (**b**) the RTTOV model-simulated versus CRTM-simulated BT of the analysis from channel 11 at 0600 UTC on 13 September 2022. The red diagonal line shows the place where the RTTOV model-simulated BT is equal to the CRTM-simulated BT.

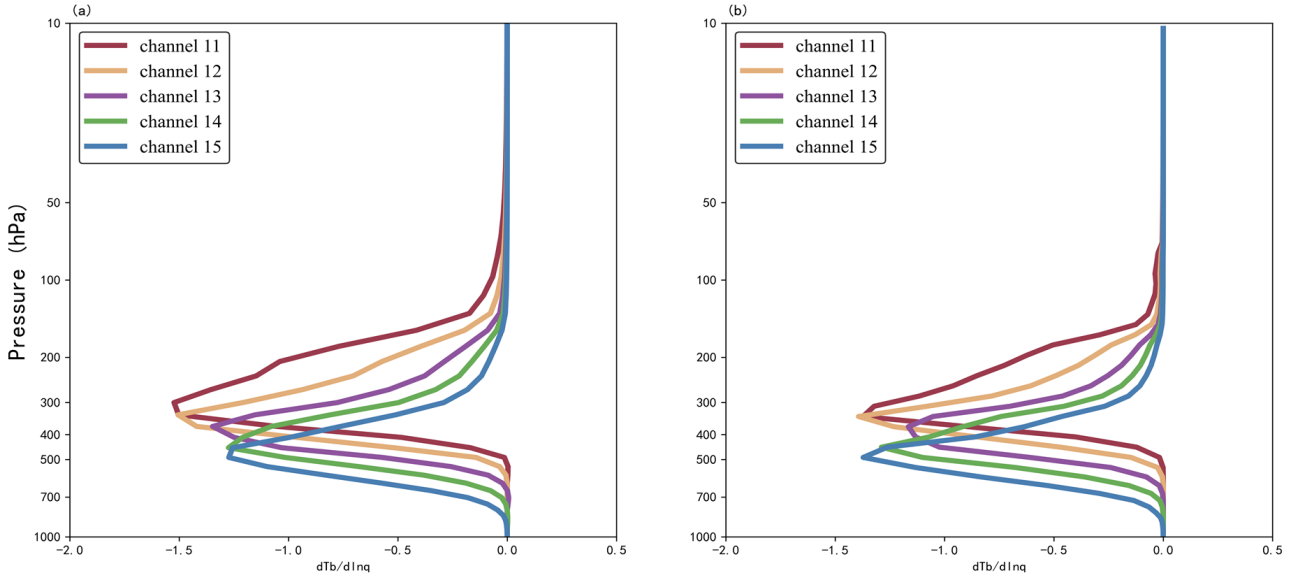


Figure 12. Jacobian functions of water vapor for channels 11, 12, 13, 14, and 15 calculated based on (**a**) the RTTOV model and (**b**) the CRTM.

5.3. Forecast Verification

5.3.1. Track Forecast

Figure 13 displays the simulated typhoon tracks from the GTS_ERA, the RTTOV model, and the CRTM along with their track errors. It is obvious that MWHS2 data assimilation with either the RTTOV model or the CRTM outperforms the GTS_ERA to some extent. The results indicate that the CRTM produces reduced typhoon track errors compared to the RTTOV model at each time, suggesting the possibility that the CRTM is able to simulate a typhoon track that is relatively closer to the observed typhoon track.

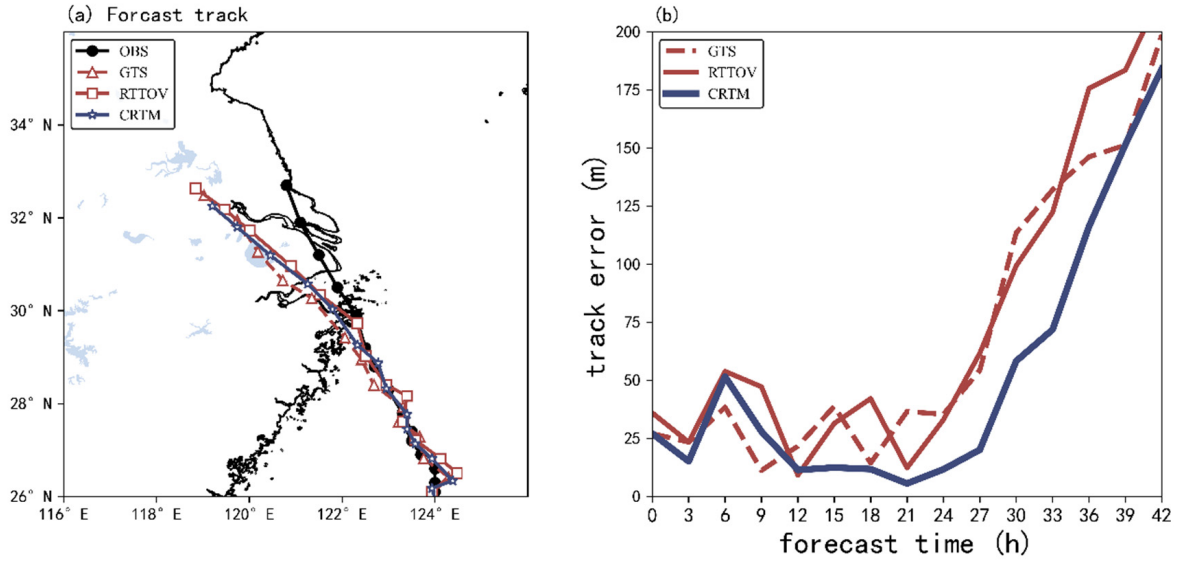


Figure 13. Track forecast (**a**) and track error (**b**) from the RTTOV model and the CRTM.

5.3.2. Intensity Forecast

Figure 14 presents the MSLP error and maximum wind speed error based on the RTTOV model and the CRTM. It can be seen that the MSLP error simulated by the CRTM is larger than that of the RTTOV model at all times, while in the last 17 h, the maximum wind speed error simulated by the CRTM is smaller than that of the RTTOV model. Unlike the track forecasts, the intensity error from both experiments with the CRTM and the RTTOV model is rather comparable.

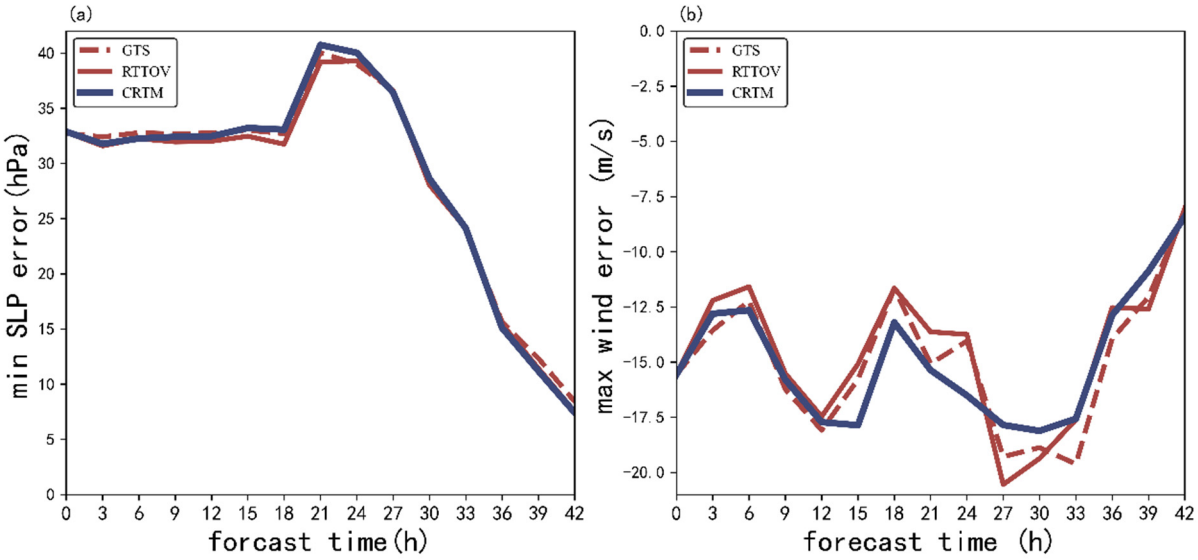


Figure 14. Same as Figure 13, but for MSLP and near-surface WS_{max}.

6. Discussion

In this study, four numerical experiments were conducted based on the WRF model and the 3DVAR system to investigate the influence of FY-3D MWHS2 radiance data on the simulation of Typhoon Muifa in 2022 under clear-sky conditions. To further study the effects of MWHS2 radiance data assimilation under different background conditions on the analyses and deterministic predictions of this typhoon case, two different sets of initial conditions based on the GFS analysis data and ERA-5 reanalysis data were selected for the experiments. Additionally, the simulation results of Typhoon Muifa were compared using the RTTOV model and the CRTM. The following conclusions are drawn:

1. Under clear-sky conditions, there is a significant reduction in notable errors in the GFS and ERA-5 background fields, and the simulated MWHS2 radiance matches better with the observations after assimilating the MWHS2 radiance data. Comparing the scatter diagrams, it is found that assimilating the FY-3D MWHS2 radiance data is efficient for the investigated typhoon case.
2. Benefiting from the assimilation of MWHS2 radiance data, the 500 hPa geopotential height and the SLP simulated using the GFS analysis data as the background field and the ERA-5 reanalysis data as the background field are improved, respectively. The horizontal wind speed and relative humidity at 850 hPa simulated by both background fields show a positive adjustment effect, although the adjustment of relative humidity simulated by the GFS background field is more apparent.
3. The assimilation of MWHS2 radiance data results in a more obvious positive adjustment effect on the typhoon track simulated using the GFS analysis data as the background field, while the positive adjustment effect on typhoon intensity is more obvious when using the ERA-5 reanalysis data as the background field.
4. It seems that the channels in the CRTM experiment are more sensitive to water vapor compared to the RTTOV experiment, when considering the total effects of all the channels. As a result, the simulated typhoon track using the CRTM slightly matches the observation better than that of the RTTOV model. However, the intensity error from both experiments with the CRTM and the RTTOV model is rather comparable.

7. Conclusions

According to the findings of this study, different initial fields will lead to different simulation and assimilation results. It seems that the typhoon intensity simulated using the GFS analysis data is more enhanced, while the typhoon track simulated using the ERA-5 reanalysis data yields less track errors. The assimilation of MWHS2 radiance data mainly corrects the near-surface wind field and sea-level pressure field simulated using the ERA-5 reanalysis data, resulting in improved typhoon intensity. On the other hand, the background based on the GFS analysis data can be corrected in terms of the relative humidity and 500 hPa geopotential height, resulting in reduced typhoon track errors. It can be seen that MWHS2 data assimilation is capable of correcting the performance of the background data accordingly. In addition, the sensitivity experiments based on different observation operators were conducted to investigate the performance of MWHS2 data assimilation. It is found that the radiance simulation characteristics based on the RTTOV model and the CRTM are similar. It seems that the data assimilation experiment with the CRTM significantly reduces the typhoon track error than the experiment with the RTTOV model does, while the intensity error from both experiments is rather comparable.

This study examined the effects of MWHS2 radiance data assimilation using different background conditions and rapid radiation transfer models on the analyses and deterministic prediction of the Super Typhoon Muifa case, although the improvement in this study may be different from operational applications. However, these conclusions are drawn based on the study of Typhoon Muifa and cannot be generalizable to other cases. Additional research is required to establish the applicability of these findings to other cases. In addition, future studies should also consider the use of all-sky assimilation with considerations of more uncertain sources and the application of more advanced assimilation

methods, such as the 4DVar method and hybrid assimilation method, to further investigate the approaches to better depict the background errors of typhoon forecasts.

Author Contributions: Conceptualization, D.X.; writing—original draft, L.H. and D.X.; writing—review and editing, H.L. and L.J.; formal analysis, L.H. and A.S.; data curation, L.J. and A.S. All authors have read and agreed to the published version of the manuscript.

Funding: This research was funded by the Chinese National Natural Science Foundation of China (G42192553), the Natural Science Foundation of China (U2242212), the Program of Shanghai Academic/Technology Research Leader (21XD1404500), and the Shanghai Typhoon Research Foundation (TFJJ202107), the Chinese National Natural Science Foundation of China (G41805016), the research project of the Institute of Atmospheric Environment, China Meteorological Administration, Shenyang in China (2020SYIAE02).

Data Availability Statement: The FY-3D MWHS2 radiance data were freely downloaded from http://satellite.nsmc.org.cn (accessed on 17 June 2023), along with the conventional observations from the National Centers for Environmental Prediction (NCEP)'s operational Global Telecommunication System (GTS) from http://rda.ucar.edu/datasets/ds337.0/ (accessed on 17 June 2023). The precipitation observations were provided by the National Meteorological Information Center of the China Meteorological Administration (CMA) (https://data.cma.cn/data/detail/dataCode/NAFP_CLDAS2.0_NRT.html) (accessed on 17 June 2023). Part of the software was associated with the National Center for Atmospheric Research (NCAR) using version 4.4 of the WRF and WRF-3DVar system. The data were provided by the NCEP Global Forecast System for the products of the $0.25^\circ \times 0.25^\circ$ GFS datasets and the European Centre for Medium-Range Weather Forecasts for the products of the $0.25^\circ \times 0.25^\circ$ ERA-5 datasets, available at https://rda.ucar.edu/datasets/ds084-1/ (accessed on 17 June 2023) and https://cds.climate.copernicus.eu/ (accessed on 17 June 2023). The figures were created with NCL version 6.6.2 from https://ncl.ucar.edu (accessed on 17 June 2023) and Python version 3.8.15 from https://www.python.org (accessed on 17 June 2023).

Acknowledgments: We acknowledge the High-Performance Computing Center of Nanjing University of Information Science & Technology for their support of this work.

Conflicts of Interest: The authors declare no conflict of interest.

References

1. Chen, L.; Li, Y.; Cheng, Z. An overview of research and forecasting on rainfall associated with landfalling tropical cyclones. *Adv. Atmos. Sci.* **2010**, *27*, 967–976. [CrossRef]
2. Wu, Z.; Alshdaifat, N.M. Simulation of marine weather during an extreme rainfall event: A case study of a tropical cyclone. *Hydrology* **2019**, *6*, 42. [CrossRef]
3. Zhang, D.; Wang, J.; Zhang, Y. Review of typhoon monitoring technology based on remote sensing satellite data. *Remote Sens. Technol. Appl.* **2014**, *28*, 994–999.
4. Bormann, N.; Duncan, D.; English, S.; Healy, S.; Lonitz, K.; Chen, K.; Lawrence, H.; Lu, Q. Growing operational use of FY-3 data in the ECMWF system. *Adv. Atmos. Sci.* **2021**, *38*, 1285–1298. [CrossRef]
5. Zou, X. Studies of FY-3 Observations over the past 10 years: A review. *Remote Sens.* **2021**, *13*, 673. [CrossRef]
6. Wang, Y.; Wang, B.; Fei, J.; Han, Y.; Ma, G. The effects of assimilating satellite brightness temperature and bogus data on the simulation of Typhoon Kalmaegi (2008). *Acta Meteorol. Sin.* **2013**, *27*, 415–434. [CrossRef]
7. Liu, C.; Gong, J. Impact of AMSU-A and MHS radiances assimilation on Typhoon Megi (2016) forecasting. *Open Geosci.* **2023**, *15*, 20220460. [CrossRef]
8. Dhanya, M.; Gopalakrishnan, D.; Chandrasekar, A.; Singh, S.K.; Prasad, V. The impact of assimilating MeghaTropiques SAPHIR radiances in the simulation of tropical cyclones over the Bay of Bengal using the WRF model. *Int. J. Remote Sens.* **2016**, *37*, 3086–3103. [CrossRef]
9. Mathur, A.; Gangwar, R.; Gohil, B.; Deb, S.K.; Kumar, P.; Shukla, M.V.; Simon, B.; Pal, P. Humidity profile retrieval from SAPHIR on-board the Megha-Tropiques. *Curr. Sci.* **2013**, *104*, 1650–1655.
10. Zhang, L.; Chen, B. Improving numerical simulation of typhoon LEKIMA (2019) through assimilating ATMS radiance data. In Proceedings of the EGU General Assembly Conference Abstracts, Vienna, Austria, 3–8 May 2020; p. 6256.
11. He, J.; Chen, H.; Zhang, S.; Li, N. Observations and Forcasting Analysis of Hurricane Sandy Using Satellite Microwave Remote Sensing. In Proceedings of the IGARSS 2019-2019 IEEE International Geoscience and Remote Sensing Symposium, Yokohama, Japan, 28 July–2 August 2019; pp. 7552–7555.
12. Yang, Y.-M.; Du, M.-B.; Zhang, J. FY-3A satellite microwave data assimilation experiments in tropical cyclone forecast. *J. Trop. Meteorol.* **2013**, *19*, 297.

13. Xu, D.; Min, J.; Shen, F.; Ban, J.; Chen, P. Assimilation of MWHS radiance data from the FY-3B satellite with the WRF Hybrid-3DVAR system for the forecasting of binary typhoons. *J. Adv. Model. Earth Syst.* **2016**, *8*, 1014–1028. [CrossRef]
14. Jiang, L.; Shi, C.; Zhang, T.; Guo, Y.; Yao, S. Evaluation of assimilating FY-3C MWHS-2 radiances using the GSI global analysis system. *Remote Sens.* **2020**, *12*, 2511. [CrossRef]
15. Lawrence, H.; Bormann, N.; Lu, Q.; Geer, A.; English, S. An evaluation of FY-3C MWHS-2 at ECMWF. In *EUMETSAT/ECMWF Fellowship Programme Research Report*; EUMETSAT/ECMWF: Reading, UK, 2015; Volume 37.
16. Lawrence, H.; Bormann, N.; Geer, A.J.; Lu, Q.; English, S.J. Evaluation and assimilation of the microwave sounder MWHS-2 onboard FY-3C in the ECMWF numerical weather prediction system. *IEEE Trans. Geosci. Remote Sens.* **2018**, *56*, 3333–3349. [CrossRef]
17. Li, J.; Liu, G. Direct assimilation of Chinese FY-3C Microwave Temperature Sounder-2 radiances in the global GRAPES system. *Atmos. Meas. Tech.* **2016**, *9*, 3095–3113. [CrossRef]
18. Chen, K.; Fan, J.; Xian, Z. Assimilation of MWHS-2/FY-3C 183 GHz channels using a dynamic emissivity retrieval and its impacts on precipitation forecasts: A southwest vortex case. *Adv. Meteorol.* **2021**, *2021*, 6427620. [CrossRef]
19. Chen, K.; Chen, Z.; Xian, Z.; Li, G. Impacts of the All-Sky Assimilation of FY-3C and FY-3D MWHS-2 Radiances on Analyses and Forecasts of Typhoon Hagupit. *Remote Sens.* **2023**, *15*, 2279. [CrossRef]
20. Xian, Z.; Chen, K.; Zhu, J. All-sky assimilation of the MWHS-2 observations and evaluation the impacts on the analyses and forecasts of binary typhoons. *J. Geophys. Res. Atmos.* **2019**, *124*, 6359–6378. [CrossRef]
21. Sun, W.; Xu, Y. Assimilation of FY-3D MWHS-2 radiances with WRF hybrid-3DVar system for the forecast of heavy rainfall evolution associated with Typhoon Ampil. *Mon. Weather. Rev.* **2021**, *149*, 1419–1437. [CrossRef]
22. Xu, D.; Shu, A.; Li, H.; Shen, F.; Li, Q.; Su, H. Effects of Assimilating Clear-Sky FY-3D MWHS2 Radiance on the Numerical Simulation of Tropical Storm Ampil. *Remote Sens.* **2021**, *13*, 2873. [CrossRef]
23. Song, L.; Shen, F.; Shao, C.; Shu, A.; Zhu, L. Impacts of 3DEnVar-Based FY-3D MWHS-2 Radiance Assimilation on Numerical Simulations of Landfalling Typhoon Ampil (2018). *Remote Sens.* **2022**, *14*, 6037. [CrossRef]
24. Shu, A.; Xu, D.; Zhang, S.; Shen, F.; Zhang, X.; Song, L. Impacts of Multi-Source Microwave Satellite Radiance Data Assimilation on the Forecast of Typhoon Ampil. *Atmosphere* **2022**, *13*, 1427. [CrossRef]
25. Li, Y.; Chen, K.; Xian, Z. Evaluation of all-Sky assimilation of FY-3C/MWHS-2 on Mei-yu precipitation forecasts over the Yangtze-Huaihe river basin. *Adv. Atmos. Sci.* **2021**, *38*, 1397–1414. [CrossRef]
26. Lucia, A.; Guo, X.; Richey, P.J.; Derebail, R. Simple process equations, fixed-point methods, and chaos. *AlChE J.* **1990**, *36*, 641–654. [CrossRef]
27. Ha, T.; Heo, K.-Y.; Jeon, J.S.; Kang, S. Numerical modelling of large swell waves using different atmospheric reanalysis data in east sea. *J. Coast. Res.* **2017**, *79*, 164–168. [CrossRef]
28. Shen, F.; Tang, C.; Xu, D.; Li, H.; Liu, R. Experiment of assimilating Doppler radar data in Typhoon Saomai based on the different initial conditions. *Haiyang Xuebao* **2021**, *43*, 69–81.
29. Li, X.; Zeng, M.; Wang, Y.; Wang, W.; Wu, H.; Mei, H. Evaluation of two momentum control variable schemes and their impact on the variational assimilation of radarwind data: Case study of a squall line. *Adv. Atmos. Sci.* **2016**, *33*, 1143–1157. [CrossRef]
30. Harris, B.; Kelly, G. A satellite radiance-bias correction scheme for data assimilation. *Q. J. R. Meteorolog. Soc.* **2001**, *127*, 1453–1468. [CrossRef]
31. Liou, Y.-A.; Liu, J.-C.; Liu, C.-C.; Chen, C.-H.; Nguyen, K.-A.; Terry, J.P. Consecutive dual-vortex interactions between quadruple typhoons Noru, Kulap, Nesat and Haitang during the 2017 North Pacific typhoon season. *Remote Sens.* **2019**, *11*, 1843. [CrossRef]
32. Grasso, L.; Lindsey, D.T.; Lim, K.-S.S.; Clark, A.; Bikos, D.; Dembek, S.R. Evaluation of and suggested improvements to the WSM6 microphysics in WRF-ARW using synthetic and observed GOES-13 imagery. *Mon. Weather. Rev.* **2014**, *142*, 3635–3650. [CrossRef]
33. Hong, S.-Y.; Lim, J.-O.J. The WRF single-moment 6-class microphysics scheme (WSM6). *Asia-Pac. J. Atmos. Sci.* **2006**, *42*, 129–151.
34. Dudhia, J. Numerical study of convection observed during the winter monsoon experiment using a mesoscale two-dimensional model. *J. Atmos. Sci.* **1989**, *46*, 3077–3107. [CrossRef]
35. Mlawer, E.J.; Taubman, S.J.; Brown, P.D.; Iacono, M.J.; Clough, S.A. Radiative transfer for inhomogeneous atmospheres: RRTM, a validated correlated-k model for the longwave. *J. Geophys. Res. Atmos.* **1997**, *102*, 16663–16682. [CrossRef]
36. Kain, J.S. The Kain–Fritsch convective parameterization: An update. *J. Appl. Meteorol.* **2004**, *43*, 170–181. [CrossRef]
37. Moradi, I.; Goldberg, M.; Brath, M.; Ferraro, R.; Buehler, S.A.; Saunders, R.; Sun, N. Performance of radiative transfer models in the microwave region. *J. Geophys. Res. Atmos.* **2020**, *125*, e2019JD031831. [CrossRef]
38. Di, D.; Ai, Y.; Li, J.; Shi, W.; Lu, N. Geostationary satellite-based 6.7 μm band best water vapor information layer analysis over the Tibetan Plateau. *J. Geophys. Res. Atmos.* **2016**, *121*, 4600–4613. [CrossRef]

Disclaimer/Publisher's Note: The statements, opinions and data contained in all publications are solely those of the individual author(s) and contributor(s) and not of MDPI and/or the editor(s). MDPI and/or the editor(s) disclaim responsibility for any injury to people or property resulting from any ideas, methods, instructions or products referred to in the content.